U.S. DEPARTMENT OF ENERGY | Office of Science

DOE/SC-ARM-21-002

# Cross-Scale Land-Atmosphere Experiment Field Campaign Report

P Gentine

February 2021

ARM

## DISCLAIMER

DOE/SC-ARM-21-002

# Cross-Scale Land-Atmosphere Experiment Field Campaign Report

P Gentine, Columbia University
Principal Investigator

February 2021

Work supported by the U.S. Department of Energy,
Office of Science, Office of Biological and Environmental Research

# Acronyms and Abbreviations

| | |
|---|---|
| ABL | atmospheric boundary layer |
| AC | alternating current |
| ARM | Atmospheric Radiation Measurement |
| DTS | distributed temperature sensing |
| FO | fiber optic |
| GPR | Gaussian Processes Regression |
| MOST | Monin-Obukhov similarity theory |
| NWP | numerical weather prediction |
| RMSE | root-mean-square error |
| SGP | Southern Great Plains |
| TKE | turbulent kinetic energy |
| USB | universal serial bus |

# Contents



# Figures

# 1.0 Study Area and Experimental Setup

The experimental setup was installed in 2017. It is located adjacent to the world's largest and most extensive climate research facility, the Southern Great Plains (SGP) atmospheric observatory, which was established by the U.S. Department of Energy's Atmospheric Radiation Measurement (ARM) user facility. This site was selected due to the abundance of environmental data that can support the proposed project. The location and layout of the experimental setup are presented in Figure 1. The site extends through two agricultural fields separated by the Coal Road. One agricultural field (hereafter called "the homogeneous site") contains a relatively homogeneous soil composition and a homogeneous alfalfa vegetation cover. The other agricultural field (hereafter called "the heterogeneous site") extends through two different soil compositions and is covered by two vegetation covers, which are different in type and coverage ratio (see Figure 1, lower part).

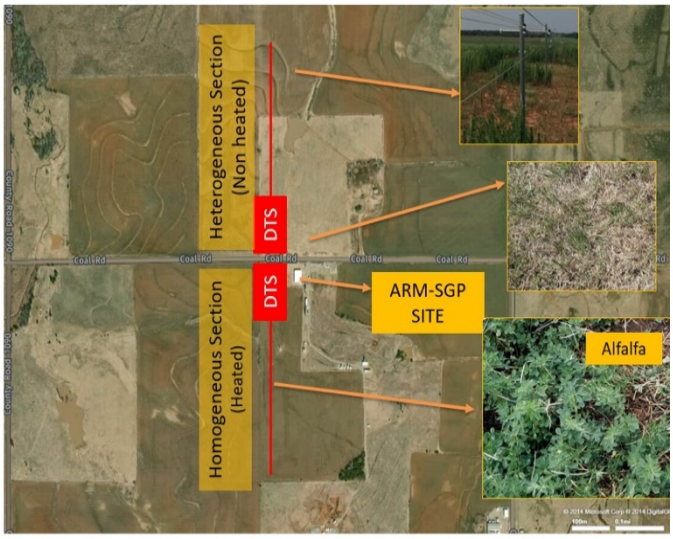


**Figure 1**. Location and layout of the experimental setup including the different observed vegetation covers.

Two distributed temperature sensing (DTS) units were installed inside air-conditioned containers on the locations marked in red in Figure 1. Each DTS unit was connected to three aerial and three ground fiber optic (FO) transects. Each transect has a length of 600 m not including the coiled sections illustrated in Figure 2. This proposal focuses only on the ground transects, which consists of three FO installed in the soil over a 45o plane and at depths of 5, 10, and 15 cm that extends over the total length of both the homogeneous and heterogeneous sites (600 m on each site). Three calibration baths are installed in each site according to the configuration presented in Figure 2. Both DTS units continuously recorded the temperature over the entire FO installations every second until May 2020.

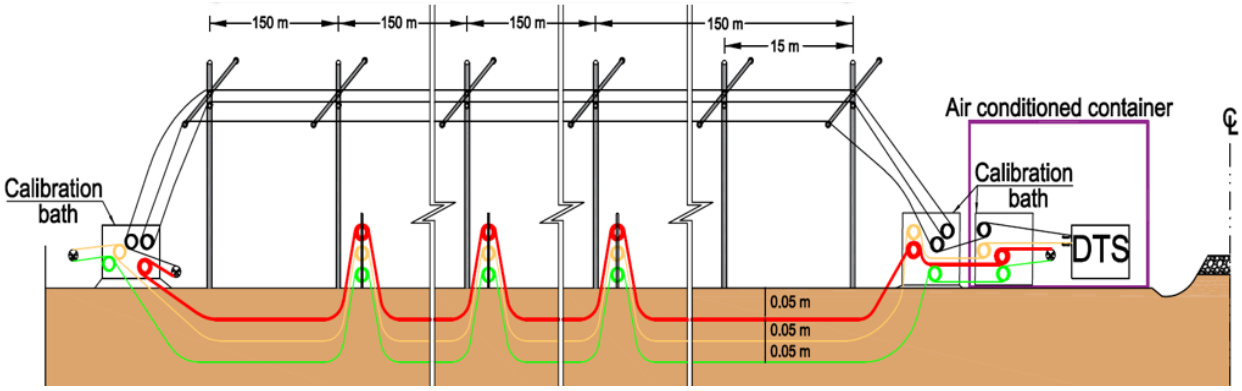


**Figure 2**. Schematic diagram of the installed FO transects in the homogenous site.

In June 2018, we revised the previous air fiber setup of 2017 by detaching the air fiber from the steel wire (Figure 3) to reduce the temperature signal due to the heat conduction at the ARM SGP site. Two sections of 600-meter-long FO cables transect were then collecting air temperature and soil temperature. We are also uploading all data generated by this experiment to the ARM Data Center at Oak Ridge National Laboratory.

**Figure 3**. The revised air fiber design in June 2018 and previous setup in 2017. Previous design: the air fiber is directly in contact with the steel wire (the uppermost steel wire in contact with air fiber). Revised design: the air fiber was separated from steel wire by plastic spacers (the middle steel wire connected with air fiber by two black spacers).

Five different soil moisture stations were installed; three along the homogeneous and two along the heterogeneous ground FO transects, respectively. Each station consists of four EC5® sensors installed at depths of 5, 10, 15, and 25 cm. Soil moisture measurements from the four sensors are recorded continuously every minute using a HOBO USB Micro Station Data Logger. Three undisturbed soil samples were taken in the location of every soil moisture station during their installation process to apply any needed soil-specific calibrations to the sensor's measurements.

In February 2020, 17 HOBOnet Soil Moisture EC5 Sensors were also installed in the homogeneous transect at the depth of the heated FO cable at the locations presented in Figure 4. The data from these

sensors were collected using a HOBO MicroRX station, which was uploaded to the HOBOnet website via a cellular connection. Soil samples were taken from the locations of the new sensors using cores that have a diameter and height of 7.62 and 15.24 cm, respectively.

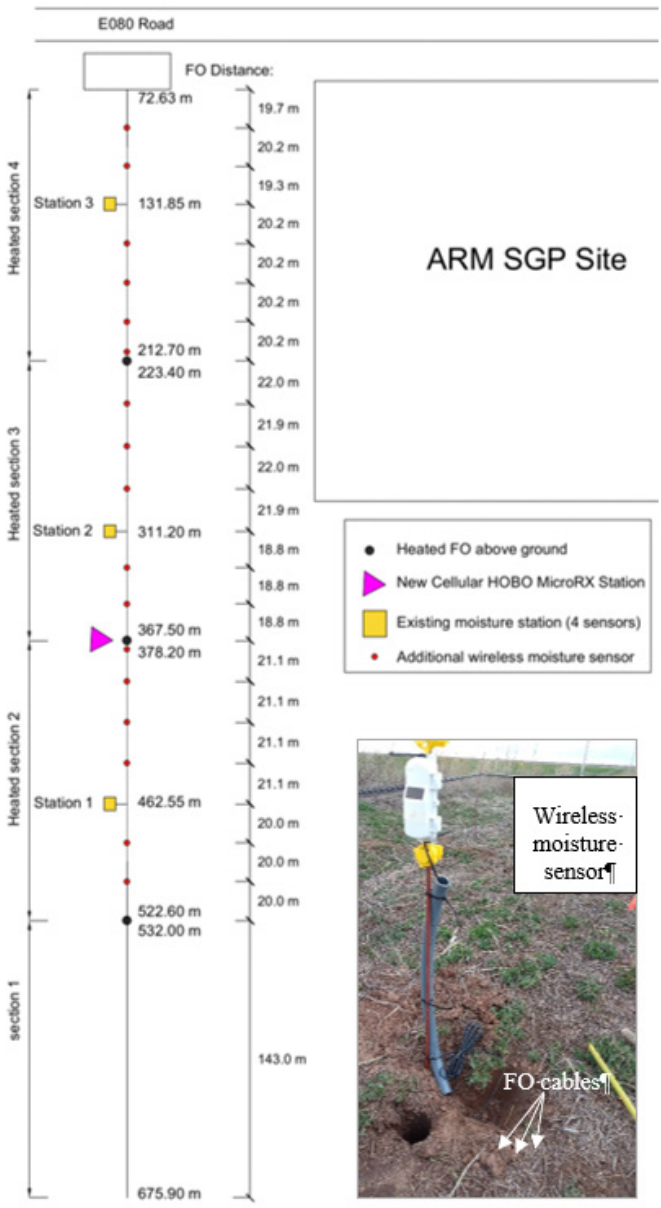


**Figure 4**. Schematic diagram of the location of the additional wireless soil moisture sensors installed in the homogenous transect in February 2020.

On 29 February, 2020 a Hydra Go handheld probe was used to map the heterogeneity in the soil moisture content of the homogeneous transect. Soil moisture content measurements were taken over a distance ranging from 3.5 to 4 m along the whole transect.

# 2.0 Heating Protocol for the Active Soil Measurements

Seven heat pulses were applied in the period from 12:30 PM to 7:00 AM daily. The heat pulses were applied only to the first 450 m of the middle ground OF cable of the homogeneous site (drawn in yellow in Figure 2). The heat pulses (eight minutes each) were applied using a MicroFUSION AC power controller (Control Concepts, Chanhassen, Minnesota) and a time-activated relay controller (NCD, Osceola, Missouri), which is used to control the timing and duration of the heat pulses.

# 3.0 Data Analysis

## 3.1 Turbulence Spectra in the Equilibrium Range of the Stable Atmospheric Boundary Layer

We have focused on the study of turbulence spectra in the stable atmospheric boundary layer (ABL). For the first time, we proposed a shape of the turbulent kinetic energy (TKE) and temperature spectra in horizontal wavenumber for the equilibrium range (Figure 5) that consists of three regimes at small Froude number: the buoyancy subrange, a transition region, and the isotropic inertial subrange through dimensional analysis and substantial revision of previous theoretical approximation (Weinstock 1978). Our field observation provides unique spatial observation without invoking Taylor's frozen turbulence hypothesis (Taylor 1938) and supports the proposed spectral scaling (Figure 5) in addition to various eddy-covariance observations.

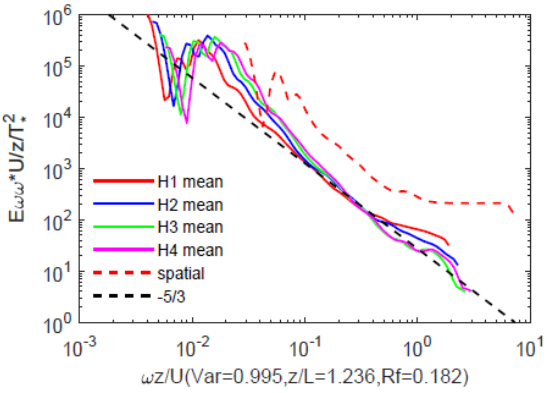


**Figure 5**. Spatial spectra and spatial mean of temporal spectra of temperature along fiber optics in representative 30-minute periods of DTS data in the stable atmospheric boundary layer. Only the buoyancy subrange and transition region are resolved due to limited temporal resolution and temporal averaging. $\boldsymbol{E_{\omega\omega}}$ is wavelet spectrum in frequency, $\boldsymbol{U}$ is mean streamwise wind velocity, $\boldsymbol{z}$ is measurement height above ground, $\boldsymbol{T_*}$ is scaling temperature, $\boldsymbol{\omega = 2\pi f}$ is angular frequency, $\boldsymbol{Var}$ is variance of temperature, $\boldsymbol{L}$ is Obukhov length, and $\boldsymbol{R_f}$ is flux Richardson number. "H1 mean", "H2 mean", "H3 mean", and "H4 mean" denotes the spatial mean of temporal spectra at four fiber optic measurement heights (1.00 m, 1.25 m, 1.50 m, and 1.75 m) respectively. Taken from Cheng et al. 2020a.

This study provides a clear explanation for the failure of Monin-Obukhov similarity theory (MOST; Monin and Obukhov 1954) in very stable atmospheric boundary layers. The buoyancy scale (Billant and Chomaz 2001) characterizing the transition region is not considered in MOST, thus leading to a failure

when calculating turbulent fluxes in very stable conditions at $k_O > k_a$, where $k_O$ denotes the wavenumber corresponding to the Dougherty-Ozmidov scale (Dougherty 1961, Ozmidov 1965) and $k_a$ denotes the wavenumber for wall effects (Katul et al. 2014, Townsend 1976), as shown in Figure 6. The study thus suggests developing new turbulence parameterization by explicitly adding the buoyancy scale to MOST, which should contribute to improved stably stratified turbulence representation in numerical weather prediction (NWP) and climate models (Svensson et al. 2011).

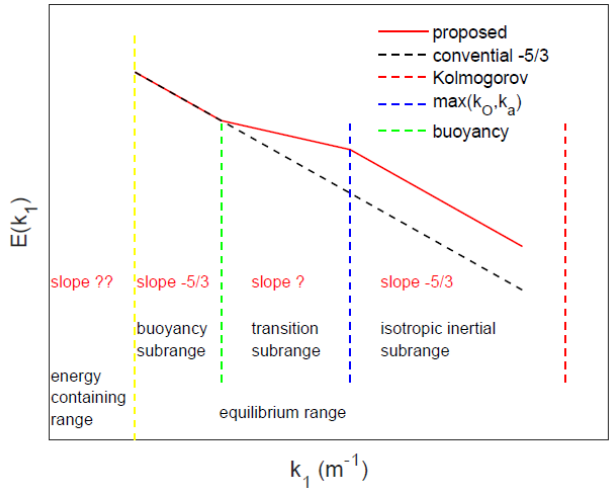


**Figure 6**. Schematic of turbulent kinetic energy and temperature spectra in horizontal wavenumber in the stable atmospheric boundary layer. $\boldsymbol{k_1}$ is horizontal wavenumber, $\boldsymbol{E(k_1)}$ is turbulent kinetic energy or temperature spectra. $\boldsymbol{k_O}$ denotes the wavenumber corresponding to the Dougherty-Ozmidov scale. $\boldsymbol{k_a}$ denotes the wavenumber for wall effects. "Kolmogorov" denotes the Kolmogorov scale and "buoyancy" denotes the buoyancy scale. Taken from Cheng et al. 2020a.

## 3.2 Power-Law Scaling of Turbulence Cospectra in the Stable Atmospheric Boundary Layer

We examined the shape of the turbulence cospectra at high wavenumbers from extensive field measurements of wind velocity and temperature in various stably stratified atmospheric conditions at high Reynolds numbers. We show that the cospectral scaling deviates from the typically assumed -7/3 scaling proposed by Lumley (1964) and Lumley (1967) for high wavenumbers in the equilibrium range and seems to better follow a -2 power-law scaling (Figure 7) that also is valid within dimensional analysis.

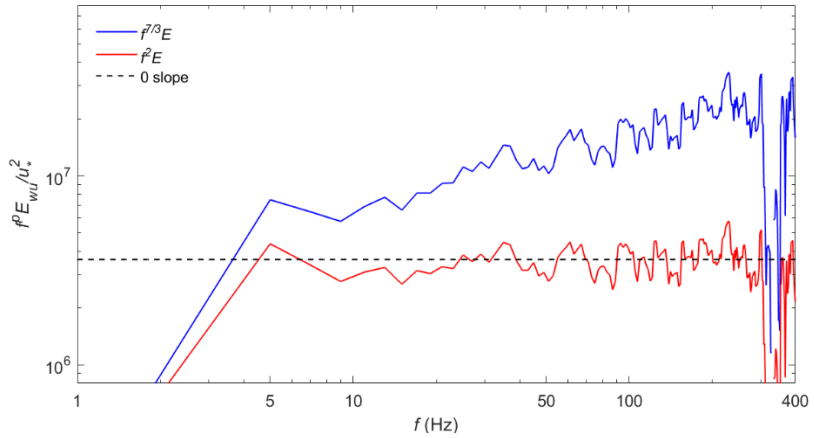


**Figure 7**. Median of normalized temporal cospectrum of momentum flux (denoted by $\boldsymbol{E_{wu}/u_*^2}$ or $\boldsymbol{E}$) multiplied by $\boldsymbol{f^{7/3}}$ (blue lines) or $\boldsymbol{f^2}$ (red lines) for each frequency in six representative 30-minute periods of MATERHORN hot film data. $\boldsymbol{p}$ is an exponent equal to 7/3 or 2 and $\boldsymbol{f}$ is sampling frequency in Hz , $\boldsymbol{E_{wu}}$ is the wavelet cospectrum of the vertical velocity $\boldsymbol{w}$ and streamwise velocity $\boldsymbol{u}$, and $\boldsymbol{u_*}$ is the friction velocity. Taken from Cheng et al. 2020b.

Our SGP field observations are consistent with previous laboratory experiments (Mydlarski 2003, Mydlarski and Warhaft 1998, Sakai et al. 2008) suggesting a $-2$ scaling for turbulence cospectra at Reynolds number as high as $R_\lambda = 582$ ($R_\lambda$ is Taylor-microscale-based Reynolds number [Pope 2000]). As for applications in the ABL, Horst (1997) assumed a $-2$ scaling for scalar flux as it approximates observations, and could be analytically computed. Here we provide multiple lines of evidence suggesting that the cospectra might obey a $-2$ scaling in the stable ABL. This correction can then be used in eddy-covariance data and should improve estimates of the fluxes.

## 3.3 Soil Measurements

This section describes the soil analysis that was performed on the data collected in the homogenous section after installing the 17 additional HOBOnet Soil Moisture EC5 Sensors and until the project ended (data collected during the three months from March to May, 2020).

Figure 8 shows the observed soil moisture at the different EC5 stations during the study period using the optical fiber corrected based on calibration to the existing probes (see later sections). It is worth noting that a severe precipitation event was observed at the site in April. This event caused an abrupt increase in soil moisture to reach near-saturation at all the stations. Many periods of substantial drydowns occurred, allowing us to assess substantial changes in soil moisture conditions and their regulation on evapotranspiration. Our following analysis will focus on the space-time organization of soil moisture, as well as the impact of soil type and small-scale heterogeneity in soil moisture. We also got in touch with the COSMO sensor team, who have installed the COSMO probe at the SGP site, measuring soil moisture with a large footprint of ~400 m. The aggregate of this footprint will be compared to the results we are obtaining at our site, in particular to understand the role of sub-kilometer-scale heterogeneity. The unique space-time structure of soil moisture will permit us to address some key questions on the spatial organization of soil moisture at sub-kilometer scale, which remains entirely unknown (soil moisture satellites are at scales ~10km), such as the role of different soil types, the role of microtopography, or the impact on local temperature.

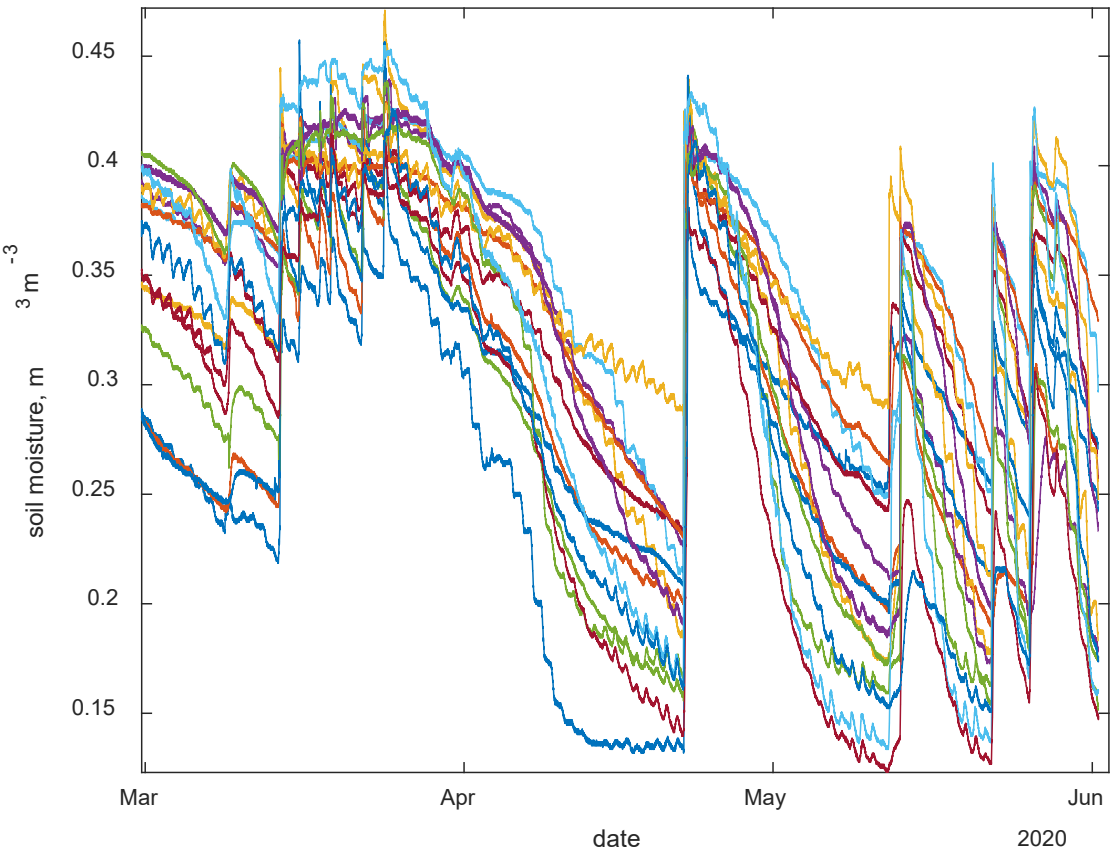


**Figure 8**. Observed soil moisture at the different EC5 stations during the study period.

### 3.3.1 DTS Data Acquisition

Each of the six 600-m transects (three aerial and three underground transects) were calibrated separately. The COVID-19 pandemic limited the ability of the site team to maintain a significant temperature difference between the three calibration baths during the study period, which is required for applying the traditional three-bath, single-calibration method of Hausner et al. (2011). Therefore, the DTS data were calibrated instead using the DTS internal calibration routine. Any drift or residual differential attenuation in the calibrated temperature for each 600-m transect were then corrected using information from two of the three calibration baths. Comparison between the calibration method used and the three-bath, single-calibration method was performed on two days where the three baths were well maintained (16 March and 13 April). The calibrated signals exhibited a mean bias (<0.01 K) and had a root-mean-square error (RMSE) that ranged from 0.5 to 0.7 K. Ambient temperature during each heat pulse was estimated by fitting a linear relationship using the data from time equal -10 to 0 and 30 to 40 minutes where the zero minutes represent the start of the applied heat pulse. The estimated ambient temperatures were subtracted from their associated temperature signals to extract the variation in temperatures caused by the applied heating event.

### 3.3.2 Estimation of Soil Thermal Conductivity

The calibrated DTS signals had a spatial resolution of 0.25 m. The soil thermal conductivity ($\lambda$) corresponding to each 0.25 m was estimated from the slope of linear relationship during the heat pulse duration between the change of temperature observed at this location and the logarithm of time, as described by the following equation (De Vries 1952, Bristow et al. 1994):

$$\Delta T \approx \left({}^{q'}/_{4\pi\lambda}\right) ln(t) + b$$

where $\Delta T$ is the temperature change due to the applied heat pulse at time $t$, $q'$ is the applied heating power, and $b$ is the intercept of the fitted line. The first few seconds of the heat pulse needed to be excluded from the fitting as their behavior deviated from the aforementioned linear relationship because of the influence of the heat source finite radius and the contact resistance between the FO cable and the surrounding soil (Bristow et al. 1994). Excluding periods of 5, 10, 20, and 30 seconds were tested to investigate the sensitivity of the resulting $\lambda_h$ to the duration of the excluded period. The analysis showed that $\lambda$ was approximately insensitive to excluded periods larger than 10 seconds.

### 3.3.3 Soil Moisture Calibration Curves

The estimated $\lambda$ at the locations of the installed soil moisture stations were combined with the observed volumetric soil moisture content ($\theta$) to establish the calibration curves at these locations as shown in Figure 9:

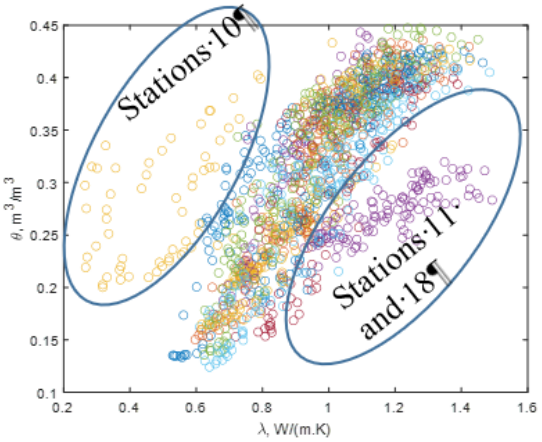


**Figure 9**. The relationship between $\boldsymbol{\lambda}$ and $\boldsymbol{\theta}$ at the locations of the 20 soil moisture stations (colors represent individual stations).

The results showed that most stations exhibited a near-similar relationship between thermal conductivity and moisture content. However, stations 1, 10, 11, and 18 showed different trends. The different behavior at station 1 was expected due to possible differences in soil characteristics as the first 10 m of the fiber-optic cable transect showed different thermal conductivity regimes and that region was heavily ponded for longer periods following any excessive precipitation event. The unexpected behavior of

station 10 was due to an animal-made ground hole that was observed next to its location. Also, the soil moisture sensor at station 18 was cut by animals after only 41 days, which indicates soil disturbance there too.

A hierarchal clustering was performed to further assess how each station was closely related to other stations with respect to $\lambda$ and $\theta$ separately. The Euclidian distance was used as the similarity measure in this analysis. The dendrograms in Figures 6 and 7 confirmed that observed $\lambda$ at stations 1, 10, and 18 were different than the other stations. Also, soil moisture estimates at stations 1, 3, 11, and 18 were different than the measurements at other stations. These results illustrate that station 1 is different, but there is a physical reason behind this difference. On the other hand, differences observed at stations 10 and 18 are purely due to disturbance to the soil column at these locations. Finally, stations 3 and 11 showed differences only with respect to soil moisture, which indicates that this difference is probably due to errors associated with the EC5 sensors at these locations. Hence, it was decided to exclude stations 10 and 18 from the analysis.

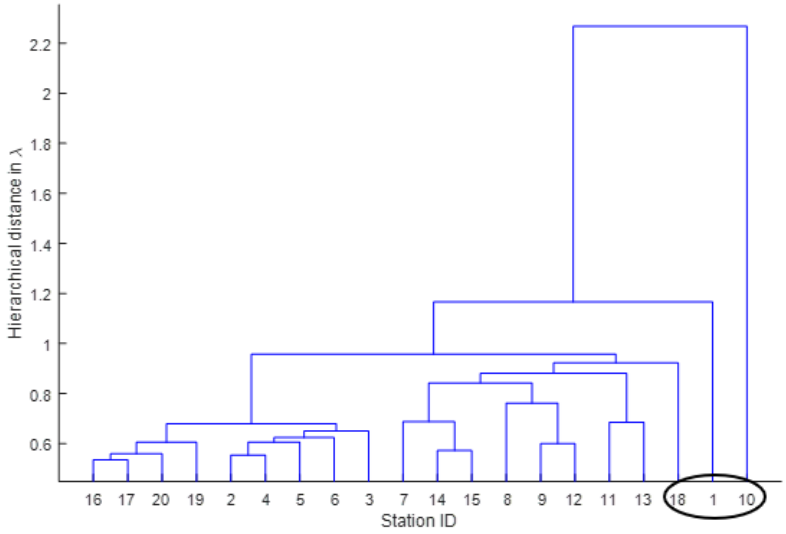


**Figure 10**. Hierarchal clustering of the 20 soil moisture stations with respect to the similarity in estimated $\boldsymbol{\lambda}$.

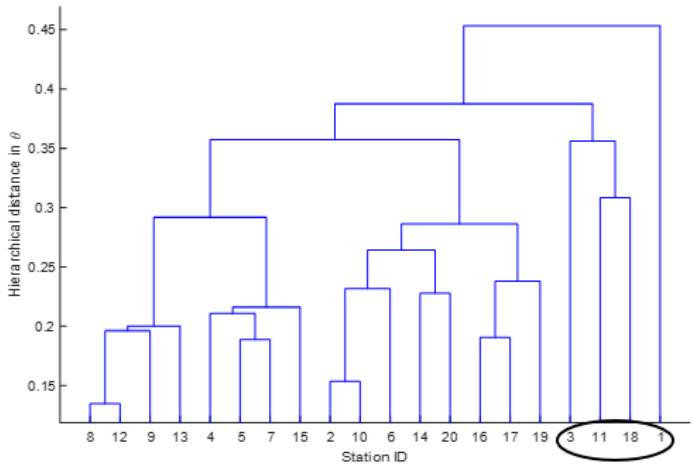


**Figure 11**. Hierarchal clustering of the 20 soil moisture stations with respect to the similarity in measured $\boldsymbol{\theta}$.

### 3.3.4 Prediction of Soil Moisture Using Machine Learning

A Gaussian Processes Regression (GPR) model was then constructed to estimate $\theta$ along the FO cable transect. The λ- $\theta$ relationships observed at the remaining EC5 soil moisture stations were used as training data. The used predictors included the distance ($d$), the observed λ, the average and maximum thermal conductivity observed at that location over the studies three months, $\lambda_{mean}$ and $\lambda_{max}$, respectively, and the average soil moisture observed at the EC5 stations ($\theta_{mean}$). The observed average ambient temperature ($T_{amb}$) was also included as a predictor. Two additional predictors representing the reduction in λ observed on the first and second day after the severe precipitation storm observed in April ($\Delta\lambda_1$ and $\Delta\lambda_2$) were also included because they correlate with the possible variation in soil characteristics over the length of the fiber-optic transect. The rational quadratic kernel was used in the GPR model. The values of the hyper-parameters were optimized using the training data.

### 3.3.5 Correction of Possible Error in $\theta$

The EC5 sensors exhibited an error of $\pm 3\%$ in estimating $\theta$. These errors could be partially responsible for the scattering observed in Figure 9. To test this hypothesis, a thermal conductivity model was fit to the data. Then the residuals were reduced by iteratively adding a random error within the EC5 $\pm 3\%$ error range to each soil moisture measurements. The Cote and Konrad (2005) model was used in this analysis. The results are presented in Figure 12. The machine-learning algorithm was run twice: Once using the raw data presented in Figure 9 after excluding the data from stations 10 and 18, and the other was based on the corrected data presented in Figure 12.

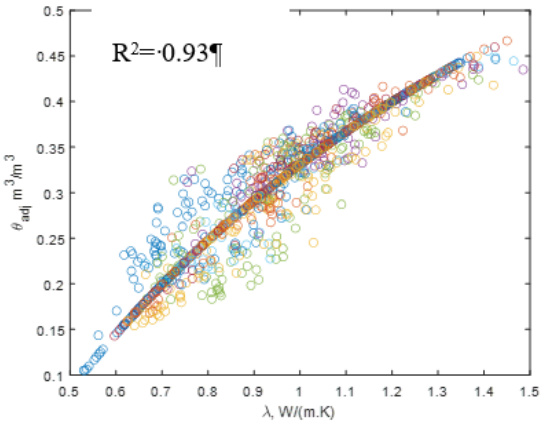


**Figure 12**. The relationship between $\boldsymbol{\lambda}$ and $\boldsymbol{\theta}$ after correcting for the possible errors in the EC5 measurements (colors represent individual stations).

### 3.3.6 Machine-Learning Model Validation

The constructed GPR models were validated by iteratively leaving out data from a single station from the training data and use the trained model to predict $\theta$ at the left-out station. The results of the GPR model trained using the raw $\theta$ showed a significant bias in the model results. Examples of the bias observed at stations 6 and 15 are presented in Figure 13. On the other hand, the model trained using the adjusted EC5 soil moisture did not suffer from that bias even when the model-validated soil moisture was compared against the raw soil moisture data (see Figure 13) and the resulting error in measurements was $\pm 5\%$ for most stations, comparable to satellite measurement error.

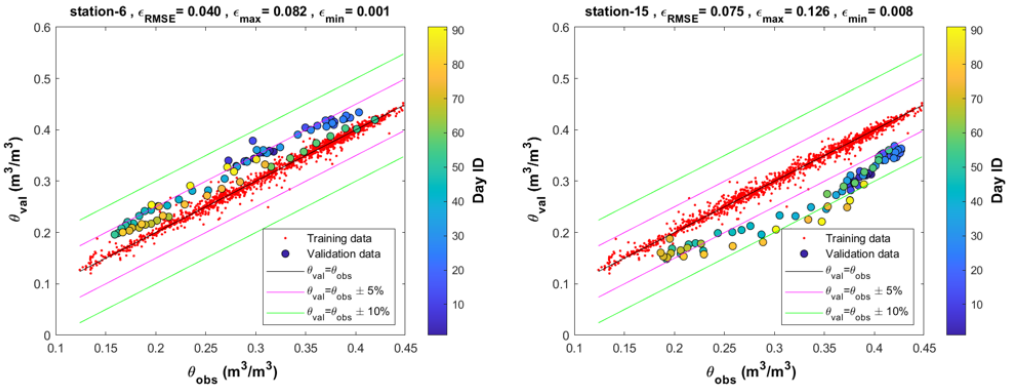


**Figure 13**. Bias in predicted soil moisture $\boldsymbol{\theta_{val}}$ estimated at stations 6 and 15 when the raw EC5 measurements were used to train the model.

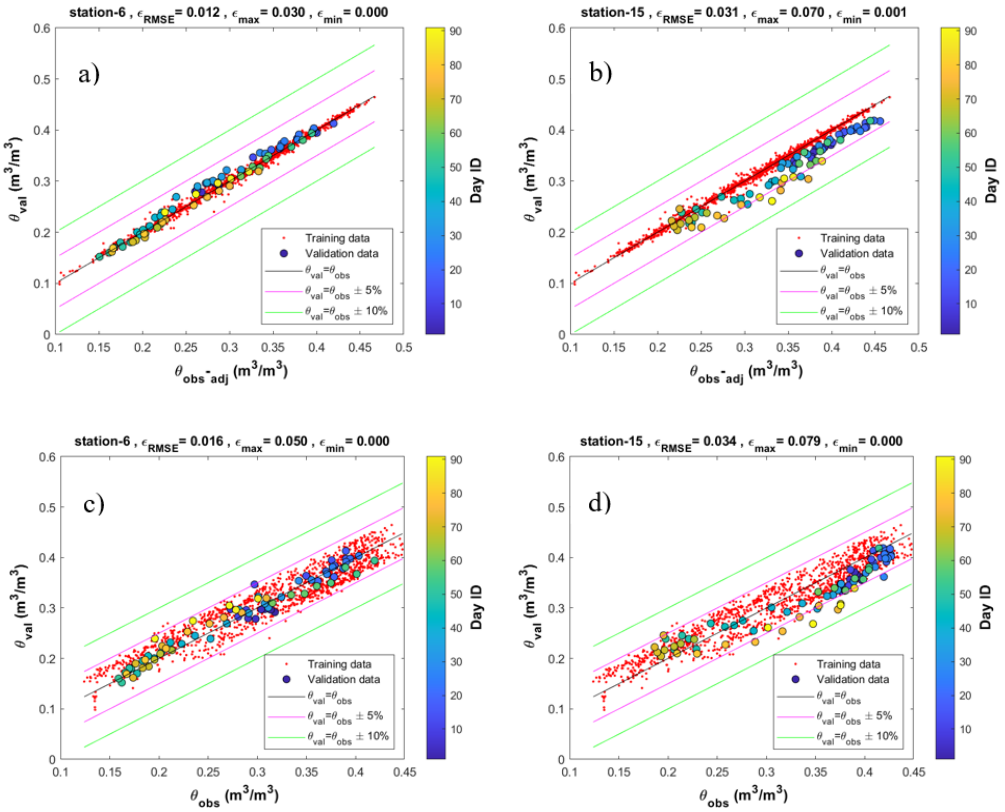


**Figure 14**. Predicted soil moisture ($\boldsymbol{\theta_{val}}$) at stations 6 and 15 against the adjusted soil moisture ($\boldsymbol{\theta_{obs-adj}}$) and raw soil moisture ($\boldsymbol{\theta_{obs}}$) when the adjusted EC5 measurements were used to train the model.

# 4.0 References

Billant, P and J-M Chomaz 2001. "Self-similarity of strongly stratified inviscid flows." *Physics of Fluids* 13(6): 1645−1651, https://doi.org/10.1063/1.1369125

Bristow KL, GJ Kluitenberg, and R Horton. 1994. "Measurement of soil thermal properties with a dual-probe heat-pulse technique." *Soil Science Society of America Journal* 58(5): 1288−1294, https://doi.org/10.2136/sssaj1994.03615995005800050002x

Cheng, Y, Q Li, A Grachev, S Argentini, HJS Fernando, and P Gentine. 2020a. "Power-law scaling of turbulence cospectra for the stably stratified atmospheric boundary layer." *Boundary-Layer Meteorology* 111(1): 1−18, https://doi.org/10.1007/s10546-020-00545-6

Cheng, Y, Q Li, S Argentini, C Sayde, and P Gentine. 2020b. "A model for turbulence spectra in the equilibrium range of the stable atmospheric boundary layer." *Journal of Geophysical Research – Atmospheres* 125(5): e2019JD032191, https://doi.org/10.1029/2019JD032191

Côté, J, and J-M Konrad. 2005. "A generalized thermal conductivity model for soils and construction materials." *Canadian Geotechnical Journal* 42(2): 443−458, https://doi.org/10.1139/t04-106

De Vries, DA. 1952. "A nonstationary method for determining thermal conductivity of soil in situ." *Soil Science* 73(2): 83−90, https://doi.org/10.1097/00010694-1952202000-00001

Dougherty, JP. 1961. "The anisotropy of turbulence at the meteor level." *Journal of Atmospheric and Terrestrial Physics* 21(2-3): 210−213, https://doi.org/10.1016/0021-9169(61)90116-7

Hausner, MB, F Suarez, KE Glander, NVD Geisen, JS Selker, and SW Tyler. 2011. "Calibrating single-ended fiber-optic Raman spectra distributed temperature sensing data." *Sensors* 1(11): 10859−10879, https://doi.org/10.3390/s11110859

Horst, TW. 1997. "A simple formula for attenuation of eddy fluxes measured with first-order-response scalar sensors." *Boundary-Layer Meteorology* 82(2): 219−233, https://doi.org/10.1023/A:1000229130034

Katul, GG, A Porporato, S Shah, and E Bou-Zeid. 2014. "The phenomenological constants explain similarity laws in stably stratified turbulence." *Physical Review* E89(2): 023007, https://doi.org/10.1103/PhysRevE.89.023007

Lumley, JL. 1964. "The spectrum of nearly inertial turbulence in a stably stratified fluid." *Journal of the Atmospheric Sciences* 21(1): 99−102, https://doi.org/10.1175/1520-0469(1964)021<0099:TSONIT>2.0.CO;2

Lumley, JL. 1967. "Similarity and the turbulent energy spectrum." *The Physics of Fluids* 10(4): 855−858, https://doi.org.10.1063/1.1762200

Monin, AS, and AM Obukhov. 1954. "Basic laws of turbulent mixing in the surface layer of the atmosphere." *Trudy geofiz. Inst. AN SSSR* 24(151): 163−187, https://gibbs.science/efd/handouts/monin_obukhov_1954.pdf.

Mydlarski, L. 2003. "Mixed velocity-passive scalar statistics in high-Reynolds-number turbulence." *Journal of Fluid Mechanics* 475: 173−203, https://doi.org/10.1017/S0022112002002756

Mydlarski, L, and Z Warhaft. 1998. "Passive scalar statistics in high-Péclet-number grid turbulence." *Journal of Fluid Mechanics* 358: 135−175, https://doi.org/10.1017/S0022112097008161

Ozmidov, RV. 1965. "On the turbulent exchange in a stably stratified ocean." *Izv. Atmos. Ocean Phys*. 1: 493−497 (English edition).

Pope, SB. 2000. *Turbulent Flows*. Cambridge University Press, Cambridge, United Kingdom.

Sakai, H, T Nordfjell, K Suadicani, B Talbot, and E Bellehuus. 2008. "Soil compaction on forest soils from different kinds of tires and tracks and possibility of accurate estimate." *Croatian Journal of Forest Engineering: Journal for Theory and Application of Forestry Engineering* 29(1): 15−27, http://crojfe.com/site/assets/files/3882/3sakai15.pd

Svensson, G, AAM Holtslag, V Kumar, T Mauritsen, GJ Steeneveld, WM Angevine, E Bazile, A Beljaars, EIF de Bruijn, A Cheng, L Conangla, J Cuxart, M Ek, MJ Falk, F Freedman, H Kitagawa, VE Larson, A Lock, J Mailhot, V Masson, S Park, J Pleim, S Soderberg, W Weng, and M Zampieri. 2011. "Evaluation of the diurnal cycle in the atmospheric boundary layer over land as represented by a variety of single-column models: The second GABLS experiment." *Boundary-Layer Meteorology* 140(2): 177−206, https://doi.org/10.1007/s10546-011-9611-7

Taylor, GI. 1938. "The spectrum of turbulence." *Proceedings of the Royal Society of London* 164(919): 476−490, https://doi.org/10.1098/rspa.1938.0032

Townsend, AA. 1976. *The Structure of Turbulent Shear Flow, Vol.2*. Cambridge University Press, Cambridge, United Kingdom, https://doi.org/10.1002/zamm.19760560921

Weinstock, J. 1978. "On the theory of turbulence in the buoyancy subrange of stably stratified flows." *Journal of the Atmospheric Sciences* 35(4): 634−649, https://doi.org/10.1175/1520-0469(1978)035<0634:OTTOTI>2.0.CO;2


www.arm.gov

U.S. DEPARTMENT OF
ENERGY

Office of Science